








Millennial-scale climate variability in the Northern Hemisphere influenced glacier dynamics in the Alps around 250,000 years ago

Vanessa Skiba ^{1,2}[✉], Christoph Spötl ³, Martin Trüssel⁴, Andrea Schröder-Ritzrau⁵, Birgit Schröder ², Norbert Frank⁵, René Eichstädter⁵, Rik Tjallingii ², Norbert Marwan ^{1,6}, Xu Zhang ^{7,8} & Jens Fohlmeister ^{1,2,9}

Mountain glaciers are sensitive recorders of natural and human-induced climate change. Therefore, it is imperative to obtain a comprehensive understanding of the interplay between climate and glacier response on both short and long timescales. Here we present an analysis of oxygen and carbon isotope data from speleothems formed mainly below a glacier-covered catchment in the Alps 300,000 to 200,000 years ago. Isotope-enabled climate model simulations reveal that $\delta^{18}\text{O}$ of precipitation in the Alps was higher by approximately 1 ‰ during interstadials compared to stadials. This agrees with interstadial-stadial amplitudes of our new speleothem-based estimate after correcting for cave-internal effects. We propose that the variability of these cave-internal effects offers a unique tool for reconstructing long-term dynamics of warm-based Alpine palaeoglaciers. Our data thereby suggests a close link between North Atlantic interstadial-stadial variability and the meltwater dynamics of Alpine glaciers during Marine Isotope Stage 8 and 7d.

¹ Potsdam Institute for Climate Impact Research (PIK), Potsdam, Germany. ² German Research Centre for Geosciences (GFZ), Potsdam, Germany. ³ Institute of Geology, University of Innsbruck, Innsbruck, Austria. ⁴ Foundation Naturerbe Karst und Höhlen Obwalden (NeKO), Alpnach, Switzerland. ⁵ Institute of Environmental Physics, Heidelberg University, Heidelberg, Germany. ⁶ Institute of Geosciences, University of Potsdam, Potsdam, Germany. ⁷ State Key Laboratory of Tibetan Plateau Earth System, Resources and Environment (TPESRE), Institute of Tibetan Plateau Research, Chinese Academy of Sciences, Beijing, China. ⁸ Alfred-Wegener-Institute (AWI), Helmholtz Centre for Polar and Marine Research, Bremerhaven, Germany. ⁹ German Federal Office for Radiation Protection (BfS), Berlin, Germany. [✉]email: skiba@pik-potsdam.de

Caves and speleothems are ubiquitous features in (carbonate-bearing) mountains worldwide, which often harbour glaciers at high elevations and/or during cold climate periods. Mountain glaciers are rapidly vanishing¹ and have been classified as a regional impact tipping element², underscoring the need to improve our understanding of their dynamics on short and long timescales.

Speleothems from the northern rim of the European Alps offer a valuable archive to investigate Northern Hemisphere glacial-interglacial climate variability and provide crucial insights into abrupt climate changes on millennial timescales^{3–16}. The Northern Alps are strongly influenced by the North Atlantic^{10,17}, a region which is thought to dictate global-scale abrupt climate events during glacial times^{18–23}. Speleothems from Alpine caves have been shown to mimic millennial-scale variability and abruptness of climate transitions known from Greenland ice cores^{4,7,9,12,13,16}. The large amplitude $\delta^{18}\text{O}$ signals captured in speleothems from the Northern Alps (in contrast to speleothems from low-elevation sites outside the Alps^{24,25}) have been attributed largely to changes in regional air temperature^{7,13}, but the detailed processes controlling these isotopic changes remain to be fully understood.

Here, we aim to resolve these processes controlling the millennial-scale isotopic changes in the high-elevation Northern Alps on interstadial-stadial (IS-S) timescales. For this, we produced a high resolution, precisely U-Th-dated speleothem multiproxy record ($\delta^{18}\text{O}$, $\delta^{13}\text{C}$, Mg/Ca and Sr/Ca) for the time span ~300 to 206 ka, i.e. covering the end of Marine Isotope Stage (MIS) 9, MIS 8, and the majority of MIS 7, from the northern rim of the Alps in central Switzerland. Speleothem records from this cave site (Melchsee-Frutt) have been found to record interstadial-stadial (IS-S) variability¹⁶ and we identify periods of pronounced IS-S variability during times of intermediate relative sea level. We use speleothem $\delta^{13}\text{C}$ data to identify periods when the cave site was likely overlain by ice in order to provide constraints on the evolution of Alpine glaciers during glacial periods where essentially no other data are available. We propose that the speleothem C isotopic composition and the Mg/Ca ratio record changes in the amount of glacier surface meltwater vs. the amount of basal meltwater occurring on Northern Hemisphere IS-S timescales. Finally, we show that IS-S amplitudes obtained from our speleothem record, after accounting for cave-internal effects, are consistent with those derived from an isotope-enabled fully-coupled ocean-atmosphere model²³ and likely reflect higher $\delta^{18}\text{O}$ values of North Atlantic seawater during interstadials compared to stadials.

Results and discussion

Interstadial-stadial variability in the Northern Alps and other European records during MIS 9–7. We present $\delta^{18}\text{O}$, $\delta^{13}\text{C}$ and Mg/Ca composite records based on three stalagmites retrieved from two high-elevation caves in the Melchsee-Frutt region of central Switzerland (46°47'N, 8°16'E; ~2000 m a.s.l.; composites produced using the *iscam* age modelling algorithm²⁶, see Supplementary Information and Figs. S1–S7 for details). We detect transitions to interstadial conditions in these records using an automatic algorithm (S-IS transitions, Fig. S8 in Supplementary Information). This algorithm is able to identify transitions based on their higher abruptness relative to other changes in the respective record. We compare our record and detected transitions to other European speleothem and sediment records (Fig. 1). The identified abrupt transitions exclusively occurred during periods of intermediate sea level (below about -30 m and above about -100 m relative to modern sea level, Fig. S9) as it was common for IS-S variability also during other glacial cycles.

Periods of occurrence and absence of abrupt S-IS transitions in the presented speleothem $\delta^{18}\text{O}$ record are corresponding to the ones from other European speleothem and sediment records (Fig. 1d–f). Additionally, these periods are also similar for more distant records including a synthetic Greenland ice-core record and a Chinese speleothem composite record (Fig. S10). Common periods of occurrence of S-IS transitions in these records are ~220–230, 240–255, 260–265 and 280–305 ka.

It is important to note that abrupt climate transitions similar to glacial S-IS transitions occurred also during MIS 7d in the Northern Alps (Melchsee-Frutt speleothems, Fig. 1a–d), in southern Europe (Italy and Spain, recorded by speleothems from Piani Eterni²⁷, Ejulve cave²⁸ and Crovassa Azzurra²⁹, Fig. 1d, e) and southeastern Europe (Lake Van^{30,31}, Turkey, Fig. 1f). MIS 7d was a cold substage during an interglacial (MIS 7) and demonstrates that relatively short periods of global cooling are sufficient to enable trigger mechanisms for S-IS transitions provided that the conditions are favourable, i.e. relative sea level is at about -60 m for MIS 7d (Fig. 1).

Alpine speleothem $\delta^{18}\text{O}$ and $\delta^{13}\text{C}$ data records palaeoglacier dynamics.

Melchsee-Frutt speleothem $\delta^{13}\text{C}$ values fall into two populations separated by the mean host rock $\delta^{13}\text{C}$ value of ~2.7 ‰ (Fig. 2). Carbon isotope values close to this value point to conditions where soil respiration was close to zero and hence soil organic matter was largely absent above the cave (cf.³³). Speleothem formation requires that host rock is dissolved by acidified water, in order to enable carbonate precipitation later in the cave. Since we infer from speleothem $\delta^{13}\text{C}$ that speleothems in this cave also grew during times of soil absence, a process other than soil respiration must have led to the acidification of the water. Previous studies suggested that oxidation of pyrite resulting in sulfuric acid can lead to host rock dissolution required for speleothem formation^{32–37}. The study area was repeatedly glaciated during the last glacial period^{38–44} and was probably also covered by a glacier during earlier glacials. Thus, it is likely that during times when signs of biological activity were absent (speleothem $\delta^{13}\text{C}$ higher than mean host rock $\delta^{13}\text{C}$), a glacier was present above the cave. Conversely, the group showing $\delta^{13}\text{C}$ values lower than the host rock value indicates some input of soil-biogenic $p\text{CO}_2$ (Fig. 2), suggestive of a climate when thin and patchy Alpine soils and sparse vegetation were present in the catchment, similar to today. Periods with soil coverage above the cave ($\delta^{13}\text{C} \leq 2.7$ ‰) are characterised by $\delta^{18}\text{O}$ values ranging from -9 to -8‰, while calcite precipitated during periods when no soil was present above the cave shows more depleted $\delta^{18}\text{O}$ values (as low as -13.5‰; Fig. 2).

We find very high $\delta^{13}\text{C}$ values (up to +12‰, Fig. 2), comparable to extreme values previously found in other Alpine speleothems (e.g., up to +20‰ in Spötl & Mangini³⁶, up to +7‰ in Spötl et al.³³). These anomalously high values cannot be explained solely by the lack of biogenic, low- $\delta^{13}\text{C}$ soil CO_2 . Instead, such high $\delta^{13}\text{C}$ values can be attributed to pyrite oxidation and resulting sulfuric acid dissolution followed by prior calcite precipitation (PCP)^{33,45} and/or rate-dependent fractionation³³. PCP comprises calcite precipitated before the drip water reaches the top of the stalagmite.

Linear regression slopes between speleothem Mg/Ca and Sr/Ca ratios can be used to detect the influence of PCP on the proxy data^{46,47} and we indeed find such evidence (Figs. S11, S12 and S13 in the Supplementary Information). Recent isotope modelling studies have found that PCP does not only affect the $\delta^{13}\text{C}$ value but can also result in changes in $\delta^{18}\text{O}$ depending on the conditions for isotopic exchange processes^{48–51}. To test this, we conducted isotope simulations using the model by Skiba and Fohlmeister⁴⁹ where we enabled isotopic exchange of $p\text{CO}_2$ and

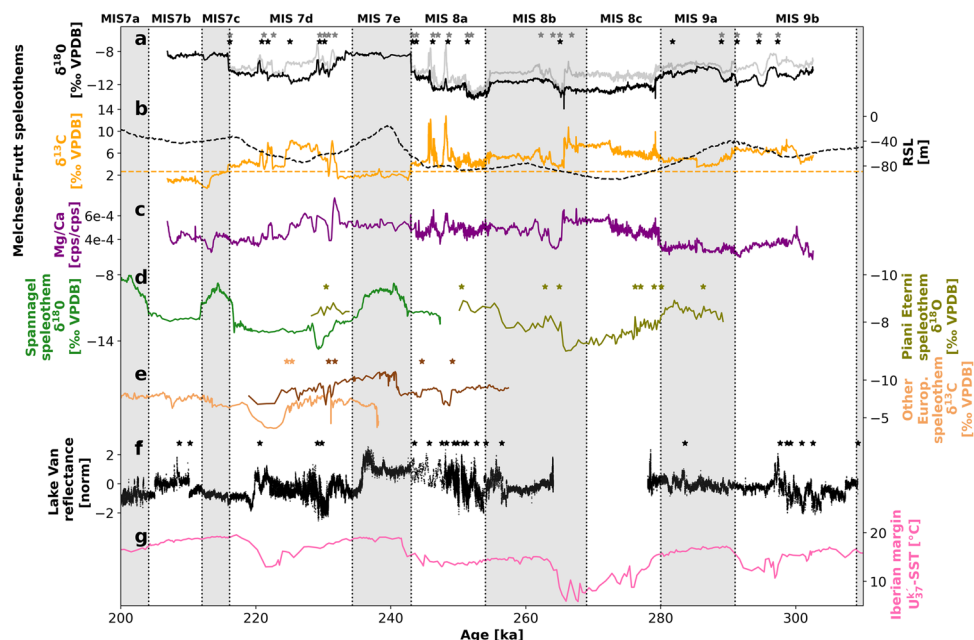


Fig. 1 Comparison of the new Alpine speleothem record with other records from Europe showing interglacial-glacial and millennial-scale (IS-S) variability. **a** Melchsee-Fruitt $\delta^{18}\text{O}$ record (grey and black are original and PCP-corrected records, see Methods and Supplementary Information for details on the PCP correction). **b** Melchsee-Fruitt $\delta^{13}\text{C}$ record (orange) and host rock $\delta^{13}\text{C}$ value indicated by the orange dashed horizontal line together with a global relative sea level (RSL) reconstruction (⁹⁶, black dashed line). **c** Melchsee-Fruitt Mg/Ca record (purple). **d** Speleothem $\delta^{18}\text{O}$ from Spannagel cave, Central Alps^{6,97}, and Pian di Eterni, Italy²⁷. **e** Speleothem $\delta^{13}\text{C}$ from Ejlulve cave, Spain²⁸ and Crovassa Azzurra, Italy²⁹. **f** Lake Van sediment core reflectance^{30,31}. **g** Iberian Margin alkenone- U_{37}^k reconstructed sea-surface temperature⁹⁸. Stars mark the detected abrupt interstadial transitions (colours correspond to time series colours, see Supplementary Information for details on transition detection method). Vertical black dashed lines mark MIS substages as indicated by their number on top of the figure (at 204.1, 212, 216.1 and 234.3⁹⁷ for MIS 7, 243, 254, 269, 280, 291 and 309 ka⁹⁹, for MIS 8 and 9).

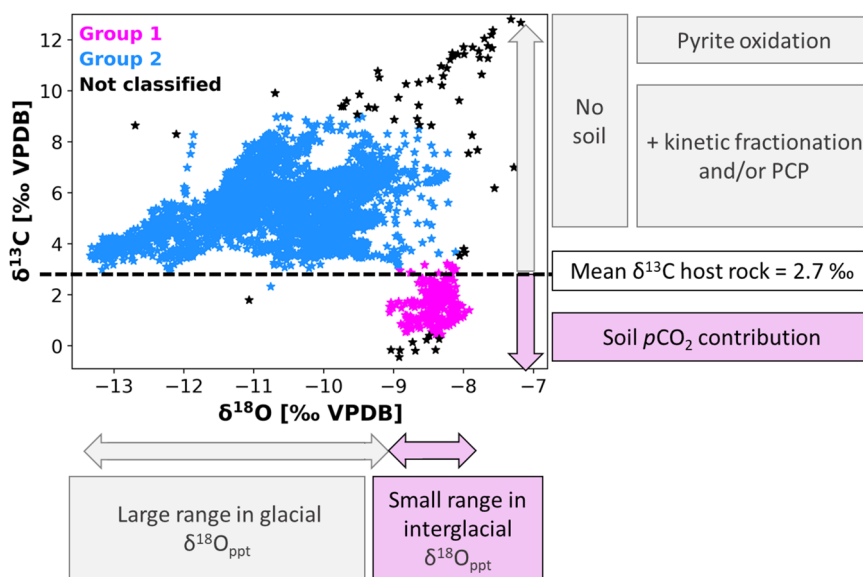


Fig. 2 Scatter plot of $\delta^{18}\text{O}$ and $\delta^{13}\text{C}$ values from Melchsee-Fruitt stalagmites. Two groups can be separated by a $\delta^{13}\text{C}$ threshold at -2.7‰ (host rock value). The DBSCAN algorithm included in the Python package scikit-learn¹⁰⁰ was used to cluster the data into groups (parameters: eps = 0.75, minimum number of points in a cluster = 330). Points are automatically assigned by the clustering algorithm where contiguous regions with high density of data points are classified as clusters and points which do not fall into such a region and do not form a contiguous region with high density of data points are not classified. Magenta stars indicate the data characterised by $\delta^{13}\text{C}$ values lower than the threshold while the majority of data is characterised by $\delta^{13}\text{C}$ values above the threshold (blue stars). Black stars mark extreme values which have not been assigned to one of the groups (74 samples).

H_2O with the bicarbonate in the drip water. We assumed a cave temperature of 3 °C (Tab. S1) and check if, after some time for PCP, exchange processes are able to bring the $\delta^{18}\text{O}$ values of the bicarbonate back to initial $\delta^{18}\text{O}$. We find that exchange processes

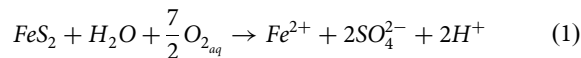
are too slow (when the PCP occurred within the cave⁴⁸) to re-equilibrate the bicarbonate isotope composition to pre-PCP values when temperatures and cave air $p\text{CO}_2$ are low as is expected for cold, high-altitude caves (Fig. S14).

We compared the PCP-sensitive Mg/Ca proxy to the $\delta^{13}\text{C}$ and $\delta^{18}\text{O}$ records to investigate whether there is a positive relationship between them which would be expected if PCP had a major impact on the isotope records. We applied a low- (>4000 yrs) and high-pass (<4000 yrs) filter on the composite records to distinguish between correlations on IS-S timescales (high-pass filtered data) and longer timescales (low-pass filtered data). Pearson correlation coefficients of low-pass filtered records are negative for $\delta^{13}\text{C}$ vs. $\delta^{18}\text{O}$ and $\delta^{18}\text{O}$ vs. Mg/Ca but positive for $\delta^{13}\text{C}$ vs. Mg/Ca (Table 1). For the high-pass filtered time series, all correlation coefficients are positive which indicates that PCP is influencing all proxies. Thus, we find that PCP is a dominant process affecting the $\delta^{13}\text{C}$, $\delta^{18}\text{O}$ and Mg/Ca proxies in the Melchsee-Frutt speleothems on IS-S timescales. However, on longer timescales $\delta^{13}\text{C}$ and Mg/Ca are as well dominated by PCP while $\delta^{18}\text{O}$ is likely predominantly reflecting broader, regional-scale $\delta^{18}\text{O}_{\text{ppt}}$ variability which results in a negative relationship with the PCP-sensitive proxies ($\delta^{13}\text{C}$ and Mg/Ca). Accordingly, we find a high and positive correlation between $\delta^{18}\text{O}$ and RSL ($r = 0.82$, $p < 0.0001$) on longer timescales (longer than 4000 yrs).

Enhanced PCP has commonly been attributed to water-limited conditions in the vadose karst system associated with a dry climate^{52–56}. However, climate model simulations suggest that interstadials were characterised by higher precipitation than stadials in the Northern Hemisphere⁵⁷ during both winter and summer, following the Clausius-Clapeyron-relationship (Fig. S15 b and c). Higher precipitation amounts lead to shorter times for PCP due to a higher availability of water in the karst system which could potentially result in decreased C and O isotope values during interstadials, contrary to what our record shows. Therefore, we suggest that the PCP variability in our Alpine speleothems reflects the extent of host rock dissolution where enhanced dissolution and, thus, higher initial Ca^{2+} concentration

in the drip water will lead to increased subsequent calcite precipitation, i.e. higher amounts of PCP (Fig. S14). It is important to note that this is independent of the amount of infiltrating water, which would solely influence the duration of PCP.

In this setting, the extent of host rock dissolution depends on the amount of pyrite oxidation. The oxidation of pyrite releases sulfate and requires the presence of water and dissolved oxygen⁵⁸:



Studies in the Swiss Alps have found that water originating from snow melt has dissolved oxygen contents of up to 60–80 % of the atmospheric value. On the contrary, water derived from glacier ice melt is usually depleted in oxygen reaching only 35–40 % with respect to the atmospheric value. This can be explained by the closer contact of snow with atmospheric O_2 ⁵⁹. Furthermore, subglacial meltwater is likely depleted in oxygen because the subglacial environment is known to host aerobic microbial communities^{59–61}. Since the extent of pyrite oxidation (and, thus, drip water Ca^{2+} concentration and the amount of PCP, Fig. S14) depends on the availability of dissolved oxygen in the water^{62,63}, we suggest that during interstadials higher amounts of water with higher O_2 content infiltrated into the karst in the caves' catchment, i.e. a higher amount of precipitation and snow melt (Fig. S15) and less meltwater from glacier basal ice. Conversely, a higher proportion of O_2 -depleted glacier meltwater entered the karst during stadial times. We reflect on alternative mechanisms and why they are unlikely to explain enhanced PCP observed during interstadials in the Method section.

Two processes could have contributed to a larger proportion of O_2 -rich water during interstadials compared to stadials (Fig. 3): (1) higher snow accumulation in winter and more summer surface meltwater due to higher summer temperatures together with higher rainfall in summer (Fig. S15), (2) larger glacier thickness during stadials, thus, lowering the melting point due to increased pressure and resulting in a higher basal meltwater contribution.

Northern Alps speleothem $\delta^{18}\text{O}$ reflects North Atlantic seawater $\delta^{18}\text{O}$. Previous studies of speleothems of glacial age in the Northern Alps suggested that the speleothem calcite $\delta^{18}\text{O}$ reflects $\delta^{18}\text{O}_{\text{ppt}}$ ^{7,13}, which today is strongly correlated with air temperature^{64,65}. Here, we present results from an isotope-enabled climate model, COSMOS-wiso (ref. 23, see “Methods”

	Low-pass filtered	High-pass filtered
$\delta^{18}\text{O}$ vs. $\delta^{13}\text{C}$	−0.34	0.74
Mg/Ca vs. $\delta^{13}\text{C}$	0.21	0.27
$\delta^{18}\text{O}$ vs. Mg/Ca	−0.06	0.23

All correlation coefficients are significant with $p < 0.001$. p -values indicate the probability that two gaussian distributed, random datasets have an absolute value of the Pearson correlation at least as high as the one computed from these datasets.

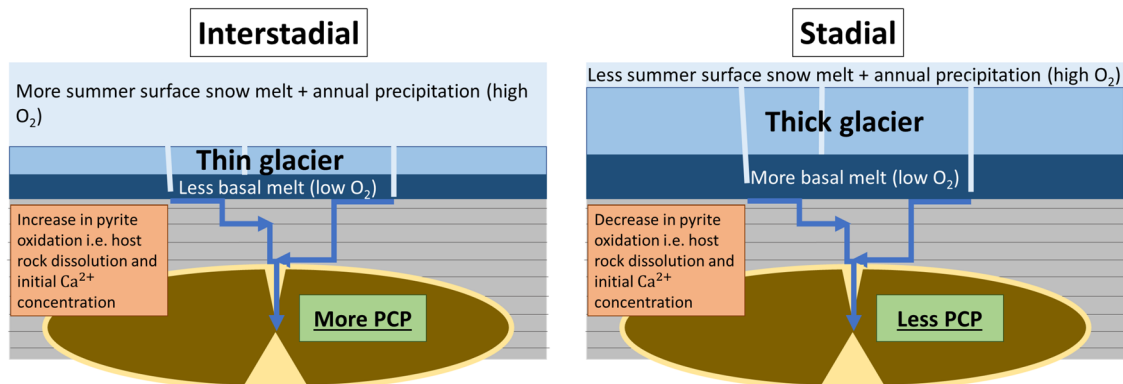


Fig. 3 Hypothesised variability of Alpine glaciers and associated input of meltwater into the subglacial karst system on IS-S timescales. Host rock and cave shown in grey and brown, respectively. During stadials a thicker glacier likely resulted in a higher contribution of O_2 -depleted basal meltwater due to the pressure-induced lowering of the melting point. Crevasse might have enabled O_2 -saturated surface meltwater to reach the base of the glacier. During interstadials, thinner ice likely increased the melting point and, thus, reduced the amount of basal meltwater contribution. Additionally, the O_2 -rich surface water contribution was likely higher due to higher precipitation together with enhanced summer meltwater (Fig. S15).

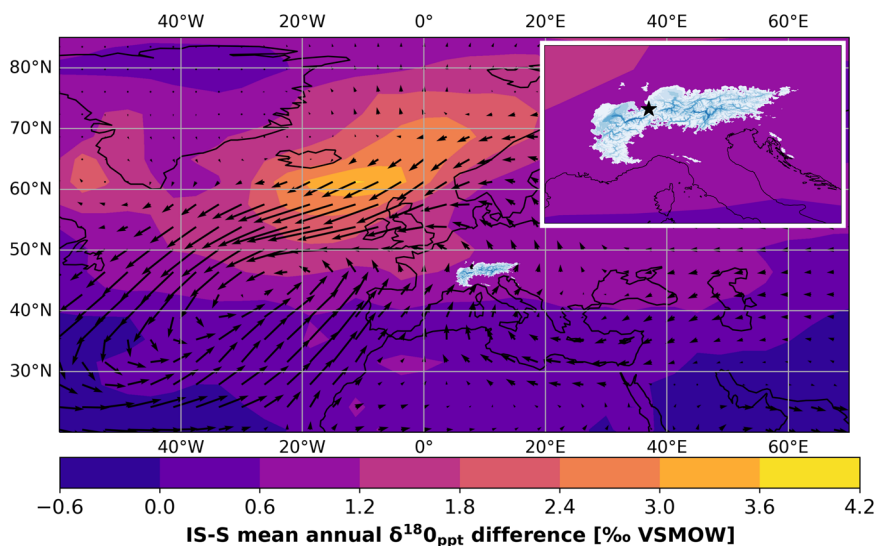


Fig. 4 Map of simulated interstitial-stadial (IS-S) difference in $\delta^{18}\text{O}$ of meteoric precipitation ($\delta^{18}\text{O}_{\text{ppt}}$) and vertically integrated moisture transport for the North Atlantic and Europe. Colour scale refers to the IS-S mean annual $\delta^{18}\text{O}_{\text{ppt}}$ difference and arrows depict the moisture transport, where longer arrows indicate larger IS-S difference. Also shown is the Last Glacial Maximum (LGM) ice extent in the European Alps⁷⁴. Inset shows enlarged Alpine LGM ice sheet and the location of the study site (Melchsee-Frutt, black star). Colour bar refers to both the main map and the inset.

section), which confirms higher $\delta^{18}\text{O}_{\text{ppt}}$ during interstadials compared to stadials for Western Europe and the North Atlantic (Fig. 4). Positive IS-S differences associated with millennial-scale AMOC oscillations²³ prevail in the North Atlantic which is the main moisture source of the Alps (area between 30 to 60°N)^{10,17}. Our model simulations suggest $\delta^{18}\text{O}_{\text{ppt}}$ values for the Alps which are 0.5 to 1.5‰ higher during interstadials compared to stadials (Fig. 4). We applied a PCP correction on the speleothem $\delta^{18}\text{O}$ (Fig. 1a, see “Methods” section and Supplementary Information for details) to obtain an improved estimate of $\delta^{18}\text{O}_{\text{ppt}}$. Indeed, after the PCP correction the amplitude of interstitial-stadial differences in speleothem calcite is close to IS-S differences found for earlier glacials^{4,7,9,12,13,16} and in model simulated $\delta^{18}\text{O}_{\text{ppt}}$ over the Alps (Fig. 4).

We find that the $\delta^{18}\text{O}_{\text{ppt}}$ IS-S difference in the Northern Alps is the result of the IS-S difference of North Atlantic surface seawater $\delta^{18}\text{O}$. Seawater $\delta^{18}\text{O}$ of the main moisture source region of the Alps (area between 30 to 60°N) was ~0.5 to 2 ‰ higher during interstadials compared to stadials (Fig. S15g), potentially due to increased evaporation. Thus, it is likely the main driver of the positive IS-S difference in simulated $\delta^{18}\text{O}_{\text{ppt}}$ over the Alps as recorded by Northern Alps speleothems. This is corroborated by $\delta^{18}\text{O}$ values of planktonic foraminifera from sediment cores in the northern and eastern North Atlantic^{66,67}. Their $\delta^{18}\text{O}$ values indicate a ~1–2‰ IS-S difference in seawater $\delta^{18}\text{O}$ when accounting for the ~10 °C calcification temperature difference on IS-S timescales, which is often found in sea surface temperature reconstructions from this region⁶⁸.

A previous study explains speleothem $\delta^{18}\text{O}$ variation on glacial and interglacial timescales by zonal shifting of the westerlies leading to enhanced moisture advected to the Northern Alps from the South during the LGM, which is depleted in $\delta^{18}\text{O}$ due to orographic rain out¹⁰. However, the COSMOS-wiso model indicates a different pattern on IS-S timescales by simulating a larger contribution of southerly-sourced moisture during warmer compared to colder periods (indicated by IS-S difference in moisture transport, Fig. 4). As this is based on simulations of one single model, further investigations should be conducted to verify this result. However, based on that we conclude that shifts in the position of the westerlies and resulting change in moisture source and pathway are unlikely to explain

the higher $\delta^{18}\text{O}_{\text{ppt}}$ over the Alps during interstadials relative to stadials.

Conclusions and Implications. The presented $\delta^{13}\text{C}$ record is punctuated with extremely positive values. They occur contemporaneously with $\delta^{18}\text{O}$ maxima. We propose that these are the result of an increased proportion of O_2 -rich annual precipitation and/or surface summer snow melt compared to a smaller proportion of O_2 -depleted glacier meltwater during interstadials relative to stadials. During interstadials, the glacier ice above the Alpine caves was increasingly melting and potentially comparably thin. This could have reduced pressure on the basal ice and thereby the melting point which would lead to less basal meltwater contribution to the karst. Larger contribution of O_2 -rich waters then enabled more pyrite to oxidise and carbonate rock to dissolve, leading to higher initial Ca^{2+} concentrations and, thus, enhanced PCP.

For stadials, speleothem $\delta^{13}\text{C}$ values indicate relatively cold conditions throughout the year resulting most likely in a comparably thick glacier. Thus, annual precipitation and/or summer snow melt amount were supposed to be small, whereas potentially relatively larger amounts of basal meltwater entered the karst (Fig. 3). Larger contribution of O_2 -depleted basal meltwater lead to reduced pyrite oxidation, resulting in less carbonate rock dissolution and decreased Ca^{2+} concentrations and, hence, reduced PCP compared to interstadials.

According to our interpretation, speleothem $\delta^{13}\text{C}$ values below the host rock $\delta^{13}\text{C}$ value of ~2.7 ‰ provide evidence of carbonate dissolution due to soil CO_2 contribution, and speleothem $\delta^{13}\text{C}$ values above ~2.7 ‰ might indicate the presence of a glacier above the cave site. Thus, the $\delta^{13}\text{C}$ speleothem record would suggest that the catchment of the caves became glaciated already at the end of MIS 9 (Fig. 1b, where $\delta^{13}\text{C}$ values show no isotopic signs of soil influence at the end of MIS 9). However, IS-S variability is only visible in the speleothem $\delta^{18}\text{O}$ and not in $\delta^{13}\text{C}$ and Mg/Ca, which suggests that changes in water sources on IS-S timescales are negligible at that time, i.e. potentially indicating the absence of a glacier. Speleothem $\delta^{13}\text{C}$ suggests that the cave site was continuously glaciated throughout MIS 8 with strong changes in meltwater contributions on IS-S timescales. During MIS 7e, c

and b the catchment was likely ice-free as suggested by the low $\delta^{13}\text{C}$ values indicating a soil C contribution. During MIS 7d, an interglacial substage, the glacier re-advanced and buried the cave site (indicated by a diminishing soil signal in speleothem $\delta^{13}\text{C}$) and we find rapid variations in $\delta^{13}\text{C}$ and PCP-corrected $\delta^{18}\text{O}$ values during MIS 7d (Fig. 1b) which we consider to result from similar mechanisms as for glacial times.

Our study provides new insights into several relevant and emerging aspects of speleothem science. We show that not only the duration for PCP, determined by the air vs. water content in the karst, but also the amount of PCP (i.e., the difference between initial Ca^{2+} of the cave drip water, which is determined by the soil $p\text{CO}_2$ and equilibrium Ca^{2+} concentrations, when the solution is in equilibrium with cave air $p\text{CO}_2$) need to be considered when interpreting speleothem stable isotope records. This has important implications for speleothem-based climate proxy interpretation. In the vast majority of studies, PCP-sensitive proxies have been interpreted to reflect the amount of infiltration based on the negative relationship between the duration of PCP and water availability in the karst system. However, the amount of PCP might follow an opposite pattern whereby wetter conditions promote soil bioproductivity⁶⁹ and, thus, increases the initial Ca^{2+} concentration of drip water with respect to equilibrium Ca^{2+} concentrations and thereby the amount of PCP.

Our data suggests a strong PCP influence not only on speleothem $\delta^{13}\text{C}$ but also on $\delta^{18}\text{O}$ which previously has been thought to be limited due to fast re-equilibration of the dissolved bicarbonate with the drip water as initially suggested by Hendy⁷⁰. Since then, more accurate equilibration times have been reported⁷¹ implying relatively slow equilibration with the drip water as demonstrated also by isotope modelling studies (refs. 48,49, Fig. S14). Oxygen isotopes are the single most extensively used speleothem-based climate proxy and are of special interest to compare with climate models simulating $\delta^{18}\text{O}_{\text{ppt}}$ ^{72,73}. We disentangled the two main signals on IS-S timescales recorded in speleothem $\delta^{18}\text{O}$ ($\delta^{18}\text{O}_{\text{ppt}}$ vs. PCP) and find a much better match with the isotope-enabled climate model IS-S differences in $\delta^{18}\text{O}_{\text{ppt}}$ after correcting for PCP. This also corroborates the isotope-enabled model results that Northern Alps $\delta^{18}\text{O}_{\text{ppt}}$ recorded in speleothem archives reflect North Atlantic seawater $\delta^{18}\text{O}$ changes on IS-S timescales, but only when accounted for PCP. Thus, it is crucial to focus future research on the impact of PCP on speleothem $\delta^{18}\text{O}$ (PCP in the vadose zone vs. on the stalactite, impact of CO_2 exchange) and advancing methods and models to disentangle the PCP component from (isotope) proxies.

If we would have not accounted for PCP in our study, climate-related $\delta^{18}\text{O}_{\text{ppt}}$ changes would have been enormously overestimated. This would be difficult to explain with climatic processes alone (e.g., interstadial speleothem $\delta^{18}\text{O}$ values as high as interglacial values, Fig. 2). However, it has to be pointed out that the effect of PCP can vary for cave and drip sites and for each case it has to be evaluated how to account for it (e.g., when PCP occurs already in the karst leaving much more time for re-equilibration⁴⁸). PCP corrections involve parameter assumptions which can also introduce errors and such corrections are not always recommended. Furthermore, the strong effect of PCP at our site is also an advantage as it results in more pronounced interstadial-stadial transitions in our speleothem isotope records and thereby improves accuracy when trying to detect them. A major uncertainty of our correction approach arises from the kinetic fractionation effect which we only approximate in our correction. This underscores the need for more laboratory experiments in order to derive robust empirical relationships for quantifying cave-internal processes in speleothem records.

Our study highlights the potential of high-elevation speleothems as an unique archive for studying palaeoglacier dynamics. Such studies of Alpine speleothems which grew during glacials should be extended to other glacials and potentially other mountain regions providing a test bed to validate models of mountain glacier dynamics on millennial to orbital timescales^{74,75}.

Methods

Stable isotope analyses. Samples for stable C and O isotope measurements were milled along the main growth axis. We hand-milled at 0.2 and 0.5 mm-resolution for M5_14_44B and M5_14_42, respectively. For 0.5 mm resolution we milled samples 0.2 mm wide to maintain a similar length of time over which each sample integrates, but at 0.5 mm steps. Stalagmite M43_401_14 was milled continuously at 0.1 and 0.3 mm-resolution. We obtained 2246, 1103 and 2113 samples for stalagmite M5_14_44B, M5_14_42 and M43_401_14, respectively. Sampling resolution for all stalagmites was guided by the changing growth rate obtained from U-Th ages (mean growth rates are 70, 49 and 42 mm/ka for M5_14_44B, M5_14_42 and M43_401_14, respectively).

Isotopes for stalagmites M5_14_44B and M5_14_42 were measured using an automated carbonate-extraction system (KIEL IV) interfaced with a MAT253 isotope ratio mass spectrometer (IRMS; ThermoFisher Scientific) at the Helmholtz Centre GFZ in Potsdam. Samples of 60–90 μg are dissolved in 103 % H_3PO_4 at 72 °C for 12 minutes and the isotopic composition was measured on the released and cryogenically purified CO_2 . Replicate analysis of reference material (NBS19) reported relative to VPDB yielded 1 sigma uncertainties of better than 0.06 ‰ for both $\delta^{18}\text{O}$ and $\delta^{13}\text{C}$. Isotope measurements of M43_401_14 were conducted using a Delta V plus IRMS at the University of Innsbruck. This mass spectrometer is linked to an on-line Gasbench II carbonate preparation system. Details on the measurement procedure can be found in Spötl and Vennemann⁷⁶. Long-term 1 sigma precision is better than 0.08‰ for both $\delta^{13}\text{C}$ and $\delta^{18}\text{O}$. All isotopic ratios are expressed in the delta notation relative to VPDB.

Trace element analyses. The elements Ca, Mg, and Sr were measured along the isotope transects of all three stalagmites using a M4 Tornado micro-XRF scanner at the Helmholtz Centre GFZ in Potsdam. Element intensities were acquired as counts per second [cps], but log-ratios of element intensities are linear functions of element concentrations and provide robust information of relative element concentrations⁷⁷ (Figs. S12 and S13). For comparison with the stable isotope data the trace elemental records were down-sampled using Gaussian Kernels with a width of 0.5 mm.

U/Th dating. Ages for all stalagmites were determined via U/Th disequilibrium dating. Sub-samples of ~200 mg were drilled along growth layers close to the growth axis (Fig. S2). A total of 16 samples were measured for stalagmite M5_14_44B, 18 for M5_14_42, and 25 for M43_401_14. Measurements were conducted with a MC-ICP-MS (ThermoFisher Neptune Plus) at Heidelberg University following the analytical protocol of Wefing et al.⁷⁸.

Samples are first dissolved, then spiked with ^{229}Th , ^{233}U , and ^{236}U and subsequently U and Th purified using wet-column chemistry with Eichrom UTEVA resin. Isotope ratios were used to calculate U-series ages according to the decay equations⁷⁹ and error propagation of statistical uncertainty. For this, ^{234}U and ^{230}Th half-lives published in Cheng et al.⁸⁰ were used. Correction for detrital contamination assumes a $^{232}\text{Th}/^{238}\text{U}$ weight ratio of

3.8 ± 1.9^{81} and ^{230}Th , ^{234}U and ^{238}U in secular equilibrium, and is minor for most samples (Tab. S2). All U and Th isotope measurements have been collected simultaneously and data was corrected for mass fractionation and tailing as mentioned by Wefing et al. ⁷⁸.

Age-depth modelling. Age-depth modelling was performed using *iscam*²⁶, a programme designed to align records from the same cave (i.e., assuming that a similar signal is recorded) into a master record, which improves the time control provided by individual time series by reducing the age uncertainties within the overlapping periods and increases signal-to-noise ratios of the combined record. The algorithm correlates dated proxy signals from several contemporaneously growing stalagmites by varying their age-depth relation within age uncertainties. It determines the most probable age-depth model and calculates the age uncertainty for the combined record. We run 30,000,000 Monte-Carlo iterations on the time series to find the best option for the age-depth realisation, i.e. the iteration with the highest correlation coefficient between both time series. Significance of the highest correlation coefficient is tested by surrogate time series, which have similar characteristics than the measured isotope records (e.g., same dating information, proxy resolution, memory of the time series²⁶).

For each iteration, we generate 2000 surrogate time series. To calculate the significance limits, we tested each of these 2000 time series in the same way as the measured time series, except that we used only 1000 randomly selected iterations due to computational constraints. For each of the 2000 artificially constructed time series, the highest correlation, found within the 1000 iterations, was used to construct a probability density function, which defines significance limits for the correlation coefficient of the measured time series. All found correlation coefficients of the best-suited age-depth realisations for the individual stacking steps exceed the 95% confidence limits. The resulting isotope records plotted over age agree perfectly with each other (Fig. S3).

Within *iscam* we applied a pointwise linear interpolation between dated depths to produce the $\delta^{18}\text{O}$ composite record. We stacked the individual $\delta^{13}\text{C}$ records to a composite record in the same way as for $\delta^{18}\text{O}$ and placed it on the age-model obtained with the $\delta^{18}\text{O}$ data. Thus, each data point in the composite records of $\delta^{18}\text{O}$ and $\delta^{13}\text{C}$ was generated by the exact same stalagmite(s) samples. The composite records are shown in Figs. S5 and S6.

PCP correction. As explained in the main text, speleothem $\delta^{18}\text{O}$ is likely strongly modified by PCP. Thus, we aimed to disentangle the speleothem $\delta^{18}\text{O}$ in its PCP and $\delta^{18}\text{O}_{\text{ppt}}$ components using the corresponding speleothem $\delta^{13}\text{C}$ as PCP proxy. Since laboratory experiments, isotope modelling (including our sensitivity test using an speleothem isotope model, see Supplementary Information, Fig. S14) and studies investigating speleothem isotope data suggest that kinetic fractionation needs to be accounted for in speleothem isotope studies^{82–87}, we utilise an estimate of the kinetic fractionation for $\delta^{18}\text{O}$ relative to the fractionation of $\delta^{13}\text{C}$ ⁸⁷ (Fig. S16, Supplementary Information for details) to correct our speleothem $\delta^{18}\text{O}$ data with an estimate of the $\delta^{13}\text{C}$ -PCP component derived from our speleothem $\delta^{13}\text{C}$ data. We apply the PCP correction on the measured speleothem $\delta^{18}\text{O}$ data for each speleothem isotope data point where the $\delta^{13}\text{C}$ value is above the host rock value (2.7 ‰). We use the $\delta^{13}\text{C}$ enrichment above the host rock value (difference to 2.7 ‰) as estimate of $\delta^{13}\text{C}$ increase solely due to PCP and convert it to the expected PCP-driven $\delta^{18}\text{O}$ enrichment using the estimate of the kinetic fractionation for $\delta^{18}\text{O}$ relative to the fractionation of $\delta^{13}\text{C}$ (Figs. S16 and S17 in the Supplementary Information).

Alternative mechanisms cannot explain enhanced PCP during interstadials. To our knowledge other mechanisms than the one proposed in the main text cannot lead to the larger degree of PCP during interstadials compared to stadials. This section is intended to discuss these other mechanisms and demonstrates that they cannot explain the data.

We expect negligible differences between interstadials and stadials in karst temperature and in infiltrating (melt-) water temperature. When a glacier covered the cave site temperatures below the glacier and in the karst must have been always close to 0 °C. Same can be expected for surface meltwater. Thus, temperature-dependent mechanisms like rate of pyrite oxidation or oxygen saturation in water can be ruled out as explanation.

Carbonate dissolution is comparatively faster than the residence time of water in the karst (saturation achieved in a few hours up to several days^{88–90}), so that equilibrium between CO_2 dissolved in the water and Ca^{2+} ions should be always attained irrespective of the hydrological conditions (except possibly for drip sites dominated by fracture flow following heavy rainfall).

Since the $\delta^{13}\text{C}$ data indicates no soil and/or vegetation above the cave during glacial times (Fig. 2), also cave air $p\text{CO}_2$ changes can likely be ruled out as a mechanism for IS-S PCP variability as near-constant atmospheric $p\text{CO}_2$ values are expected in the cave. As there is only the atmosphere as the main CO_2 reservoir, variability in cave ventilation would not result in substantial variations in cave air $p\text{CO}_2$.

Climate model simulations. To investigate responses of $\delta^{18}\text{O}_{\text{ppt}}$ to S-IS transitions during glacial periods, we used model simulation experiments from Zhang et al. ²³, which successfully simulated glacial millennial-scale climate oscillations using the climate model COSMOS-wiso. The model COSMOS-wiso is a water isotope-enabled fully-coupled atmosphere-ocean general circulation model⁹¹. The atmospheric model is ECHAM5⁹², complemented by the land surface component JSBACH⁹³, and was used at T31 resolution ($\sim 3.75^\circ$), with 19 vertical layers. The ocean model is MPI-OM⁹⁴ and includes sea-ice dynamics modelled with viscous-plastic rheology⁹⁵. It has a resolution of GR30 ($3^\circ \times 1.8^\circ$) in the horizontal, with 40 uneven vertical layers.

We chose modelling results from the experiment E40ka_Orb which characterises unforced millennial-scale changes in Atlantic Meridional Overturning Circulation under fixed glacial conditions, resembling glacial S-IS transitions. More details about experimental design can be found in Zhang et al. ²³. We show differences in meteoric precipitation $\delta^{18}\text{O}$ (Fig. 4) and seawater $\delta^{18}\text{O}$, precipitation amount and temperature over the eastern North Atlantic and Europe (annual, summer and winter) between the simulated interstadial and stadial states (IS-S, Fig. S15).

Data availability

Here published speleothem U-/Th, isotope and trace elemental data is publicly available on the NOAA paleoclimate data archive (<https://www.nccei.noaa.gov/access/paleo-search/study/38681>).

Received: 17 January 2023; Accepted: 6 November 2023;

Published online: 20 November 2023

References

1. Rounce, D. R. et al. Global glacier change in the 21st century: every increase in temperature matters. *Science* **379**, 78–83 (2023).
2. McKay, D. I. A. et al. Exceeding 1.5°C global warming could trigger multiple climate tipping points. *Science* **377**, 944–945 (2022).

3. Spötl, C., Mangini, A., Frank, N., Eichstädter, R. & Burns, S. J. Start of the last interglacial period at 135 ka: evidence from a high Alpine speleothem. *Geology* **30**, 815–818 (2002).
4. Spötl, C. & Mangini, A. Stalagmite from the Austrian Alps reveals Dansgaard–Oeschger events during isotope stage 3: implications for the absolute chronology of Greenland ice cores. *Earth Planet. Sci. Lett.* **203**, 507–518 (2002).
5. Spötl, C., Mangini, A. & Richards, D. A. Chronology and paleoenvironment of Marine Isotope Stage 3 from two high-elevation speleothems, Austrian Alps. *Quat. Sci. Rev.* **25**, 1127–1136 (2006).
6. Spötl, C., Scholz, D. & Mangini, A. A terrestrial U/Th-dated stable isotope record of the Penultimate Interglacial. *Earth Planet. Sci. Lett.* **276**, 283–292 (2008).
7. Boch, R. et al. NALPS: a precisely dated European climate record 120–60 ka. *Clim. Past* **7**, 1247–1259 (2011).
8. Fohlmeister, J., Vollweiler, N., Spötl, C. & Mangini, A. COMNISPA II: update of a mid-European isotope climate record, 11 ka to present. *The Holocene* **23**, 749–754 (2013).
9. Moseley, G. E. et al. Multi-speleothem record reveals tightly coupled climate between central Europe and Greenland during Marine Isotope Stage 3. *Geology* **42**, 1043–1046 (2014).
10. Luetscher, M. et al. North Atlantic storm track changes during the Last Glacial Maximum recorded by Alpine speleothems. *Nat. Commun.* **6**, 1–6 (2015).
11. Häuselmann, A. D. et al. Timing and nature of the penultimate deglaciation in a high alpine stalagmite from Switzerland. *Quat. Sci. Rev.* **126**, 264–275 (2015).
12. Moseley, G. E. et al. Termination-II interstadial/stadial climate change recorded in two stalagmites from the north European Alps. *Quat. Sci. Rev.* **127**, 229–239 (2015).
13. Moseley, G. E. et al. NALPS19: Sub-orbital-scale climate variability recorded in northern Alpine speleothems during the last glacial period. *Clim. Past* **16**, 29–50 (2020).
14. Wilcox, P. S., Honiat, C., Trüssel, M., Edwards, R. L. & Spötl, C. Exceptional warmth and climate instability occurred in the European Alps during the Last Interglacial period. *Commun. Earth Environ.* **1**, 57 (2020).
15. Spötl, C., Koltai, G., Jarosch, A. H. & Cheng, H. Increased autumn and winter precipitation during the Last Glacial Maximum in the European Alps. *Nat. Commun.* **12**, 1–9 (2021).
16. Fohlmeister, J. et al. The role of Northern Hemisphere summer insolation for millennial-scale climate variability during the penultimate glacial. *Commun. Earth Environ.* **4**, 245 (2023).
17. Sodemann, H. & Zubler, E. Seasonal and inter-annual variability of the moisture sources for Alpine precipitation during 1995–2002. *Int. J. Climatol.* **30**, 947–961 (2010).
18. Alley, R. B. & Clark, P. U. The deglaciation of the Northern Hemisphere: a global perspective. *Annu. Rev. Earth Planet. Sci.* **27**, 149–182 (1999).
19. Alley, R. B., Anandakrishnan, S. & Jung, P. Stochastic resonance in the North Atlantic. *Paleoceanography* **16**, 190–198 (2001).
20. Ganopolski, A. & Rahmstorf, S. Rapid changes of glacial climate simulated in a coupled climate model. *Nature* **409**, 153–158 (2001).
21. Petersen, S. V., Schrag, D. P. & Clark, P. U. A new mechanism for Dansgaard–Oeschger cycles. *Paleoceanography* **28**, 24–30 (2013).
22. Dokken, T. M., Nisancioglu, K. H., Li, C., Battisti, D. S. & Kissel, C. Dansgaard–Oeschger cycles: interactions between ocean and sea ice intrinsic to the Nordic seas. *Paleoceanography* **28**, 491–502 (2013).
23. Zhang, X. et al. Direct astronomical influence on abrupt climate variability. *Nat. Geosci.* **14**, 819–826 (2021).
24. Genty, D. et al. Precise dating of Dansgaard–Oeschger climate oscillations in western Europe from stalagmite data. *Nature* **421**, 833–837 (2003).
25. Weber, M. et al. Evidence of warm and humid interstadials in central Europe during early MIS 3 revealed by a multi-proxy speleothem record. *Quat. Sci. Rev.* **200**, 276–286 (2018).
26. Fohlmeister, J. A statistical approach to construct composite climate records of dated archives. *Quat. Geochronol.* **14**, 48–56 (2012).
27. Columbu, A., Sauro, F., Lundberg, J., Drysdale, R. & Waele, J. de. Palaeoenvironmental changes recorded by speleothems of the southern Alps (Piani Eterni, Belluno, Italy) during four interglacial to glacial climate transitions. *Quat. Sci. Rev.* **197**, 319–335 (2018).
28. Pérez-Mejías, C. et al. Abrupt climate changes during Termination III in Southern Europe. *Proc. Natl Acad. Sci. USA* **114**, 10047–10052 (2017).
29. Columbu, A. et al. A long record of MIS 7 and MIS 5 climate and environment from a western Mediterranean speleothem (SW Sardinia, Italy). *Quat. Sci. Rev.* **220**, 230–243 (2019).
30. Stockhecke, M. et al. Chronostratigraphy of the 600,000 year old continental record of Lake Van (Turkey). *Quat. Sci. Rev.* **104**, 8–17 (2014).
31. Stockhecke, M. et al. Millennial to orbital-scale variations of drought intensity in the Eastern Mediterranean. *Quat. Sci. Rev.* **133**, 77–95 (2016).
32. Spötl, C., Fohlmeister, J., Cheng, H. & Boch, R. Modern aragonite formation at near-freezing conditions in an alpine cave, Carnic Alps, Austria. *Chem. Geol.* **435**, 60–70 (2016).
33. Atkinson, T. C. Growth mechanisms of speleothems in castleguard cave, Columbia Icefields, Alberta, Canada. *Arct. Alp. Res.* **15**, 523–536 (1983).
34. Spötl, C., Mangini, A., Bums, S. J., Frank, N. & Pavuza, R. In *Studies of Cave Sediments*, pp. 243–256 (Springer, 2004).
35. Holzkämper, S., Mangini, A., Spötl, C. & Mudelsee, M. Timing and progression of the Last Interglacial derived from a high alpine stalagmite. *Geophys. Res. Lett.* **31**, <https://doi.org/10.1029/2003GL019112> (2004).
36. Spötl, C. & Mangini, A. Speleothems and paleoglaciers. *Earth Planet. Sci. Lett.* **254**, 323–331 (2007).
37. Bajo, P. et al. Stalagmite carbon isotopes and dead carbon proportion (DCP) in a near-closed-system situation: an interplay between sulphuric and carbonic acid dissolution. *Geochim. Cosmochim. Acta* **210**, 208–227 (2017).
38. Preusser, F., Blei, A., Graf, H. & Schlüchter, C. Luminescence dating of Würmian (Weichselian) proglacial sediments from Switzerland: methodological aspects and stratigraphical conclusions. *Boreas* **36**, 130–142 (2007).
39. Graf, H. R. *Stratigraphie von Mittel- und Spätpleistozän in der Nordschweiz* (Bundesamt für Landestopografie, 2009).
40. Gaar, D., Lowick, S. E. & Preusser, F. Performance of different luminescence approaches for the dating of known-age glaciofluvial deposits from northern Switzerland. *Geochronometria* **41**, 65–80 (2014).
41. Reber, R. et al. Timing of retreat of the Reuss Glacier (Switzerland) at the end of the Last Glacial Maximum. *Swiss J. Geosci.* **107**, 293–307 (2014).
42. Gaar, D., Graf, H. R. & Preusser, F. New chronological constraints on the timing of Late Pleistocene glacier advances in northern Switzerland. *E&G Quat. Sci. J.* **68**, 53–73 (2019).
43. Kamleitner, S. et al. The Ticino-Toce glacier system (Swiss-Italian Alps) in the framework of the Alpine Last Glacial Maximum. *Quat. Sci. Rev.* **279**, 107400 (2022).
44. Kamleitner, S. et al. Last Glacial Maximum glacier fluctuations on the northern Alpine foreland: Geomorphological and chronological reconstructions from the Rhine and Reuss glacier systems. *Geomorphology* **423**, 108548 (2023).
45. Owen, R. *Development And Application Of Speleothem-based Proxies For Past Climate Change* (University of Oxford, 2017).
46. Sinclair, D. J. et al. Magnesium and strontium systematics in tropical speleothems from the Western Pacific. *Chem. Geol.* **294**, 1–17 (2012).
47. Wassenburg, J. A. et al. Calcite Mg and Sr partition coefficients in cave environments: Implications for interpreting prior calcite precipitation in speleothems. *Geochim. Cosmochim. Acta* **269**, 581–596 (2020).
48. Deininger, M. et al. Are oxygen isotope fractionation factors between calcite and water derived from speleothems systematically biased due to prior calcite precipitation (PCP)? *Geochim. Cosmochim. Acta* **305**, 212–227 (2021).
49. Skiba, V. & Fohlmeister, J. Contemporaneously growing speleothems and their value to decipher in-cave processes—A modelling approach. *Geochim. Cosmochim. Acta* **348**, 381–396 (2023).
50. Guo, W. & Zhou, C. Patterns and controls of disequilibrium isotope effects in speleothems: Insights from an isotope-enabled diffusion-reaction model and implications for quantitative thermometry. *Geochimica et Cosmochimica Acta* **267**, 196–226 (2019).
51. Sade, Z., Hegyi, S., Hansen, M., Scholz, D., & Halevy, I. The effects of drip rate and geometry on the isotopic composition of speleothems: Evaluation with an advection-diffusion-reaction model. *Geochimica et cosmochimica acta* **317**, 409–432 (2022).
52. Fairchild, I. J. et al. Controls on trace element (Sr–Mg) compositions of carbonate cave waters: implications for speleothem climatic records. *Chem. Geol.* **166**, 255–269 (2000).
53. Fairchild, I. J. et al. Modification and preservation of environmental signals in speleothems. *Earth-Sci. Rev.* **75**, 105–153 (2006).
54. Fairchild, I. J. & McMillan, E. A. Speleothems as indicators of wet and dry periods. *Int. J. Speleol.* **36**, 2 (2007).
55. Fairchild, I. J. & Treble, P. C. Trace elements in speleothems as recorders of environmental change. *Quat. Sci. Rev.* **28**, 449–468 (2009).
56. Fohlmeister, J. et al. Bunker Cave stalagmites: an archive for central European Holocene climate variability. *Clim. Past* **8**, 1751–1764 (2012).
57. Fohlmeister, J. et al. Global reorganization of atmospheric circulation during Dansgaard–Oeschger cycles. *Proc. Natl Acad. Sci. USA* **120**, e2302283120 (2023).
58. Moses, C. O., Nordstrom, D. K., Herman, J. S. & Mills, A. L. Aqueous pyrite oxidation by dissolved oxygen and by ferric iron. *Geochim. Cosmochim. Acta* **51**, 1561–1571 (1987).
59. Brown, G. H., Tranter, M., Sharp, M. J., Davies, T. D. & Tsiouris, S. Dissolved oxygen variations in Alpine glacial meltwaters. *Earth Surf. Process. Landf.* **19**, 247–253 (1994).

60. Tranter, M. et al. Geochemical weathering at the bed of Haut Glacier d'Arolla, Switzerland—a new model. *Hydrol. Process.* **16**, 959–993 (2002).
61. Tranter, M., Skidmore, M. & Wadham, J. Hydrological controls on microbial communities in subglacial environments. *Hydrol. Process.* **19**, 995–998 (2005).
62. Wunderly, M. D., Blowes, D. W., Frind, E. O. & Ptacek, C. J. Sulfide mineral oxidation and subsequent reactive transport of oxidation products in mine tailings impoundments: a numerical model. *Water Resour. Res.* **32**, 3173–3187 (1996).
63. Molson, J. W., Fala, O., Aubertin, M. & Bussi re, B. Numerical simulations of pyrite oxidation and acid mine drainage in unsaturated waste rock piles. *J. Contaminant Hydrol.* **78**, 343–371 (2005).
64. Rozanski, K., Araguas-Araguas, L. & Gonfiantini, R. Relation between long-term trends of oxygen-18 isotope composition of precipitation and climate. *Science* **258**, 981–985 (1992).
65. Kaiser, A. et al. *Links Between Meteorological Conditions And Spatial/temporal Variations In Long-term Isotope Records From The Austrian Precipitation Network* (2002).
66. McManus, J. F., Oppo, D. W. & Cullen, J. L. A 0.5-million-year record of millennial-scale climate variability in the North Atlantic. *Science* **283**, 971–975 (1999).
67. Margari, V. et al. The nature of millennial-scale climate variability during the past two glacial periods. *Nat. Geosci.* **3**, 127–131 (2010).
68. Salgueiro, E. et al. Temperature and productivity changes off the western Iberian margin during the last 150 ky. *Quat. Sci. Rev.* **29**, 680–695 (2010).
69. Orchard, V. A. & Cook, F. J. Relationship between soil respiration and soil moisture. *Soil Biol. Biochem.* **15**, 447–453 (1983).
70. Hendy, C. H. The isotopic geochemistry of speleothems—I. The calculation of the effects of different modes of formation on the isotopic composition of speleothems and their applicability as palaeoclimatic indicators. *Geochim. Cosmochim. Acta* **35**, 801–824 (1971).
71. Beck, W. C., Grossman, E. L. & Morse, J. W. Experimental studies of oxygen isotope fractionation in the carbonic acid system at 15, 25, and 40°C. *Geochim. Cosmochim. Acta* **69**, 3493–3503 (2005).
72. Comas-Bru, L. et al. Evaluating model outputs using integrated global speleothem records of climate change since the last glacial. *Clim. Past* **15**, 1557–1579 (2019).
73. B hler, J. C. et al. Comparison of the oxygen isotope signatures in speleothem records and iHadCM3 model simulations for the last millennium. *Clim. Past* **17**, 985–1004 (2021).
74. Jouv t, G. et al. Coupled climate-glacier modelling of the last glaciation in the Alps. *J. Glaciol.* **1**–15 (2023).
75. Seguinot, J. et al. Modelling last glacial cycle ice dynamics in the Alps. *The Cryosphere* **12**, 3265–3285 (2018).
76. Sp tl, C. & Vennemann, T. W. Continuous-flow isotope ratio mass spectrometric analysis of carbonate minerals. *Rapid Commun. Mass Spectrom.* **17**, 1004–1006 (2003).
77. Weltje, G. J. & Tjallingii, R. Calibration of XRF core scanners for quantitative geochemical logging of sediment cores: theory and application. *Earth Planet. Sci. Lett.* **274**, 423–438 (2008).
78. Wefing, A.-M. et al. High precision U-series dating of scleractinian cold-water corals using an automated chromatographic U and Th extraction. *Chem. Geol.* **475**, 140–148 (2017).
79. Ludwig, K. R. & Titterton, D. M. Calculation of $^{230}\text{Th}/\text{U}$ isochrons, ages, and errors. *Geochim. Cosmochim. Acta* **58**, 5031–5042 (1994).
80. Cheng, H. et al. Improvements in ^{230}Th dating, ^{230}Th and ^{234}U half-life values, and U–Th isotopic measurements by multi-collector inductively coupled plasma mass spectrometry. *Earth Planet. Sci. Lett.* **371**, 82–91 (2013).
81. Wedepohl, K. H. The composition of the continental crust. *Geochim. Cosmochim. Acta* **59**, 1217–1232 (1995).
82. Mickler, P. J. et al. Stable isotope variations in modern tropical speleothems: Evaluating equilibrium vs. kinetic isotope effects. *Geochim. Cosmochim. Acta* **68**, 4381–4393 (2004).
83. Dietzel, M., Tang, J., Leis, A. & K hler, S. J. Oxygen isotopic fractionation during inorganic calcite precipitation—Effects of temperature, precipitation rate and pH. *Chem. Geol.* **268**, 107–115 (2009).
84. Kluge, T. & Affek, H. P. Quantifying kinetic fractionation in Bunker Cave speleothems using $\Delta 47$. *Quat. Sci. Rev.* **49**, 82–94 (2012).
85. Watkins, J. M., Nielsen, L. C., Ryerson, F. J. & DePaolo, D. J. The influence of kinetics on the oxygen isotope composition of calcium carbonate. *Earth Planet. Sci. Lett.* **375**, 349–360 (2013).
86. Watkins, J. M., Hunt, J. D., Ryerson, F. J. & DePaolo, D. J. The influence of temperature, pH, and growth rate on the $\delta^{18}\text{O}$ composition of inorganically precipitated calcite. *Earth Planet. Sci. Lett.* **404**, 332–343 (2014).
87. Hansen, M., Scholz, D., Sch ne, B. R. & Sp tl, C. Simulating speleothem growth in the laboratory: determination of the stable isotope fractionation ($\delta^{13}\text{C}$ and $\delta^{18}\text{O}$) between H_2O , DIC and CaCO_3 . *Chem. Geol.* **509**, 20–44 (2019).
88. Buhmann, D. & Dreybrodt, W. The kinetics of calcite dissolution and precipitation in geologically relevant situations of karst areas: 2. *Closed Syst. Chem. Geol.* **53**, 109–124 (1985).
89. Dreybrodt, W. & Scholz, D. Climatic dependence of stable carbon and oxygen isotope signals recorded in speleothems: from soil water to speleothem calcite. *Geochim. Cosmochim. Acta* **75**, 734–752 (2011).
90. Larson, E. B. & Emmons, R. V. Dissolution of carbonate rocks in a laboratory setting: rates and textures. *Minerals* **11**, 605 (2021).
91. Werner, M. et al. Glacial–interglacial changes in H_2^{18}O , HDO and deuterium excess—results from the fully coupled ECHAM5/MPI-OM Earth system model. *Geosci. Model Dev.* **9**, 647–670 (2016).
92. Roeckner, E. et al. The atmospheric general circulation model ECHAM 5. PART I: Model description. *Report/Max-Planck-Institut f r Meteorologie*. Vol. 349 (2003).
93. Brovkin, V., Raddatz, T., Reick, C. H., Claussen, M. & Gayler, V. Global biogeophysical interactions between forest and climate. *Geophys. Res. Lett.* **36**, 1–5 (2009).
94. Marsland, S. J., Haak, H., Jungclaus, J. H., Latif, M. & R ske, F. The Max-Planck-Institute global ocean/sea ice model with orthogonal curvilinear coordinates. *Ocean Model.* **5**, 91–127 (2003).
95. Hibler, W. D. III A dynamic thermodynamic sea ice model. *J. Phys. Oceanogr.* **9**, 815–846 (1979).
96. Grant, K. M. et al. Sea-level variability over five glacial cycles. *Nat. Commun.* **5**, 1–9 (2014).
97. Wendt, K. A., Li, X., Edwards, R. L., Cheng, H. & Sp tl, C. Precise timing of MIS 7 substages from the Austrian Alps. *Clim. Past* **17**, 1443–1454 (2021).
98. Martrat, B. et al. Four climate cycles of recurring deep and surface water destabilizations on the Iberian margin. *Science* **317**, 502–507 (2007).
99. Railsback, L. B., Gibbard, P. L., Head, M. J., Voarintsoa, N. R. G. & Toucanne, S. An optimized scheme of lettered marine isotope substages for the last 1.0 million years, and the climatostratigraphic nature of isotope stages and substages. *Quat. Sci. Rev.* **111**, 94–106 (2015).
100. Pedregosa, F. et al. Scikit-learn: machine learning in Python. *J. Mach. Learn. Res.* **12**, 2825–2830 (2011).

Acknowledgements

Financial support for this research was provided by the Deutsche Forschungsgemeinschaft through grant FO809/6-1 to J.F.; X.Z. acknowledges funding from the National Science Foundation of China (no. 42075047). The MC-ICPMS facility at Heidelberg University was funded equally through the DFG instrumentation fund INST 35-1143-1 FUGG and the structure and innovation fund of Baden W rttemberg. We thank Sylvia Pinkerneil, Nicolai Klitscher and Brian Brademann from German Research Centre (GFZ) and Manuela Wimmer from University of Innsbruck for their help with laboratory work. We are grateful to Rebecca Caspani for her help during field work. We confirm that carbonate samples were collected in a responsible manner and in accordance with relevant permits and local laws.

Author contributions

V.S. and J.F. developed the concept and designed the study. A.S.-R., R.E., N.F., V.S. and J.F. prepared samples for U–Th dating, performed the measurements and assessed data quality. B.P., C.S., V.S. and J.F. performed the stable isotope measurements. M.T., C.S., J.F. and V.S. retrieved samples from the cave. V.S. and J.F. conducted calcite isotope model simulations. X.Z. performed climate model simulations. R.T. conducted trace elemental measurements. N.M. contributed to statistical analyses. All authors were involved in data interpretation and writing of the manuscript.

Funding

Open Access funding enabled and organized by Projekt DEAL.

Competing interests

The authors declare no competing interests.

Additional information

Supplementary information The online version contains supplementary material available at <https://doi.org/10.1038/s43247-023-01083-y>.

Correspondence and requests for materials should be addressed to Vanessa Skiba.

Peer review information *Communications Earth and Environment* thanks the anonymous reviewers for their contribution to the peer review of this work. Primary Handling Editors: Yama Dixit and Ali nor Lavergne.

Reprints and permission information is available at <http://www.nature.com/reprints>

Publisher's note Springer Nature remains neutral with regard to jurisdictional claims in published maps and institutional affiliations.



Open Access This article is licensed under a Creative Commons Attribution 4.0 International License, which permits use, sharing, adaptation, distribution and reproduction in any medium or format, as long as you give appropriate credit to the original author(s) and the source, provide a link to the Creative Commons licence, and indicate if changes were made. The images or other third party material in this article are included in the article's Creative Commons licence, unless indicated otherwise in a credit line to the material. If material is not included in the article's Creative Commons licence and your intended use is not permitted by statutory regulation or exceeds the permitted use, you will need to obtain permission directly from the copyright holder. To view a copy of this licence, visit <http://creativecommons.org/licenses/by/4.0/>.

© The Author(s) 2023